# City Research Online

## City, University of London Institutional Repository

# Modelling and design of low-power, non-conventional current sensors based on smart materials for high-voltage transmission lines

**B Nikolic**[*] and **S H Khan**

School of Science and Technology, City, University of London, London, EC1V 0HB, United Kingdom

E-mail: bojan.nikolic.1@city.ac.uk

## Abstract

This paper presents a new technique for measurement of current based on magnetic shape memory (MSM) smart alloys. MSM alloys undergo shape changes when exposed to magnetic fields. The non-conventional instrument transformer (NCIT) proposed in this paper utilises this property to measure current. There is a correlation between the magnetic field produced by a current and the shape change of an MSM material (MSM sensor). By exploiting this correlation, we have shown that it is possible to measure alternating currents (a.c.) in high voltage overhead transmission lines. A change in the length of the MSM element causes voltage output in a linear variable differential transducer. The design of the NCIT was optimised for transmission lines. Several designs of its magnetic circuit were simulated using finite element package ANSYS APDL. Several key parameters were investigated to evaluate their effects on the sensitivity of the NCIT. Results are presented as the relationship between the current in the conductor and strain (linear elongation) of the MSM element. A commonly used conductor in high-voltage transmission lines was modelled together with the MSM element and the magnetic circuit. Recommendations have been made on the design of NCITs considering various parameters. In addition, analyses of errors in ANSYS models for the magnetic circuit have been presented. The developed methodology and obtained results are verified by comparing them to the results obtained through an experiment done by a manufacturer of MSM materials.

Keywords: magnetic shape memory alloys, finite element modelling, non-conventional instrument transformer, overhead transmission lines

(Some figures may appear in colour only in the online journal)

[*] Author to whom any correspondence should be addressed.

## 1. Introduction

Conventional instrument transformers are transformers with an iron core for measuring current and voltage. On the other hand, so-called non-conventional instrument transformers (NCIT) are usually transformers without ferromagnetic core or with a core made of some materials that have a better response to fast changing signals than the standard iron.

NCITs have attracted a lot of attention recently. One of the main reasons for it is their design flexibility, which provides full compatibility with modern digital equipment. In contrast, this constitutes one of the major disadvantages of conventional instrument transformers. This makes NCITs suitable for many applications.

The focus of our research is on current measurement. The existence of many devices and principles for current measurement nowadays, as well as many research papers on this topic, show that there are still many problems and challenges that need to be resolved and overcome. Some of the proposed measurement principles have already found industrial applications, but majority of them are still being explored [1–7]. The main characteristics of optical sensors, Rogowski coil sensors, magnetic sensors and Hall-effect sensors are summarised in [8].

We propose a novel approach for current measurement in high-voltage (HV) transmission lines using smart materials—the magnetic shape memory (MSM) alloys. These alloys change their shape and undergo very large strain when subjected to external magnetic fields. The basic principle of the proposed NCIT is based upon the proportionality between the strain, $\varepsilon$ produced by an MSM element which is subjected to a magnetic field, $B$ produced by the current, $I$ whose magnitude is being measured. Consequently, the strain produced by the MSM element is proportional to the current in the conductor. This strain can be measured by measuring the output voltage $V$ generated by the linear variable differential transformer (LVDT) which is connected to the MSM element and is proportional to the strain produced.

In [8–10], the focus was on establishing the critical magnetic field that was needed to trigger an MSM element. In this paper we have carried out further studies to take into account significant changes that take place within an MSM element during its elongation. Based on this, we are now able to determine the upper limits of measurement range and propose a new design of our NCIT.

MSM alloys are relatively new 'smart' materials which elongate when subjected to external magnetic fields. They have very large magnetic field induced strain, more than one order of magnitude higher than maximum strains produced by conventional magnetostrictive and piezoelectric materials reaching strains of well-known thermal shape memory alloys [11–13].

The main weaknesses of MSM alloys are related to their temperature sensitivity and magneto-mechanical hysteresis. They can operate until the temperature reaches 60 °C–80 °C at which point they go through martensite-austenite transformation [14]. The so-called twinning stress is related to their temperature sensitivity and hysteresis.

There are two types of boundaries inside MSM materials: type I and type II. Twinning stress of MSM materials with type I boundaries depends on temperature, but this is not the case for MSM materials with type II boundaries. Twinning stress is considerably high for the former ones, but it is low for the latter ones which are less studied [15]. MSM materials with type II boundaries, thus have very low hysteresis and good temperature stability which is of great interest for future sensor applications.

MSM crystals have a different strain-magnetic field relationship at different pre-stress levels (loads) [16]. The best option for this NCIT application would be MSM elements which follow the curve at a load of 0.5 N mm$^{-2}$ [10]. In comparison to the other curves, this curve has the lowest threshold for triggering the MSM element (reversibly) under magnetic field and it has the largest strain.

## 2. Characteristics of the modelled conductor

Many different types of conductors are used for overhead transmission lines. An overview of most common conductors used in Europe, as well as their main properties, can be found in standard EN50182 [17]. Aluminium conductor steel reinforced (ACSR) is the most commonly used conductor at the HV level and above. The main reasons for it are well-established production capabilities (and thus favourable productions costs), but also its mechanical characteristics such as its mechanical strength. This conductor has the highest value of ampacity of all the overhead-line conductors used in the UK [17].

For these reasons we modelled ACSR conductors, specifically, 528-Al1/69-ST1A conductors (old code MOOSE) shown in figure 1. By doing minor changes in the source code that we had developed, the other types of conductors could be easily modelled in a similar way. Table 1 shows the parameters used to model this conductor.

For this research, a conductor for overhead transmission lines having ampacity higher than 2.5 kA has not been found [17–19]. Current density values in conductors in normal and the most economical working regime lie between 0.5–1 A mm$^{-2}$ and the conductor radii are in the range from 1.5–1.75 cm [18–20].

## 3. Design and optimisation of sensor for current measurement

The previous research has indicated that the MSM element is not sensitive enough to be used alone for the measurement of a.c. in high voltage overhead transmission lines in the normal working regime. This can be overcome by including a magnetic circuit to NCIT's design so the magnetic field around the current-carrying conductor is concentrated and directed towards the MSM element. It was shown in [9] and [10] that the most suitable design for this NCIT is the rectangular magnetic circuit with rounded corners made of Hiperco 50 material (figure 1).

**Table 1.** Parameters of 528-Al1/69-ST1A (old code MOOSE) conductor used for its modelling [17].

| | Number of strands | Diameter of a strand (mm) | Conductivity (S m$^{-1}$) | Relative magnetic permeability | Diameter of core (mm) | Total diameter (mm) | Total area (mm$^2$) |
|---|---|---|---|---|---|---|---|
| Steel strands | 7 | 3.53 | $5.21 \times 10^6$ | 100 | 10.6 | | |
| Aluminium strands | 54 | 3.53 | $3.54 \times 10^7$ | 1 | | | |
| Total | 61 | | | | | 31.8 | 597 |
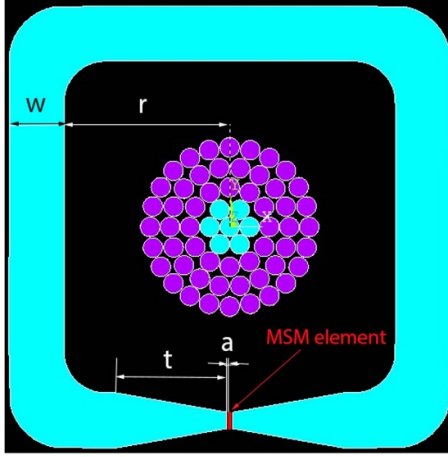


**Figure 1.** Parameters of NCIT's magnetic circuit geometry.

It is very important to carefully consider the magnetic circuit geometry as it affects sensitivity to high temperatures from the current-carrying conductor, the circuit's saturation point and, crucially, the triggering threshold of the MSM element. Whereas there is not much flexibility in the size of the MSM element, there are flexibilities in the design of the magnetic circuit, especially in terms of its geometry and distance from the conductor.

Many parameters need to be considered in order to optimise the magnetic circuit geometry for the intended use of NCIT (figure 1). These parameters include: size of the airgap, $a$ (the airgap between the poles and the MSM element), the distance from the airgap to the point where the poles start to taper, $t$, magnetic circuit's width, $w$, and position of the magnetic circuit relative to the conductor (distance between the centre of the conductor and the inner side of the magnetic circuit, $r$.

Firstly, we changed the size of the airgap with the goal to determine the variations of magnetic field amplitude on the surface of the MSM element, $B_{surface}$, and the maximum value of the magnetic field inside the magnetic circuit, $B_{max}$ in those cases. The values of all the other aforementioned parameters were kept constant. The results obtained are presented in table 2.

$B_{surface}$ (%) and $B_{max}$ in magnetic circuit (%) show a percentage change in comparison to the case when the airgap is the smallest ($a = 0.1$ mm).

The results show that even a small increase in the airgap significantly decreases $B_{surface}$. To increase the sensitivity of NCIT, the airgap size needs to be as small as it is possible. Due to the technological limitations, the airgap cannot be smaller than 0.1 mm so that size is the best option.

The overall diameter of the modelled conductor, 528-Al1/69-ST1A, is 31.8 mm, therefore, the magnetic circuit around the conductor can only be at the distance $r > 15.9$ mm. On the one hand, the magnetic circuit should be placed as close as possible to the conductor because flux density on the surface of the MSM element decreases significantly as the distance from the conductor increases. On the other hand, it is better to place it further away from the conductor as MSM element saturates at higher magnetic fields and, thus increase the upper limit of the measured current range. Furthermore, as characteristics of the magnetic circuit are affected by the heat around the current-carrying conductor, the circuit should be placed far enough from the conductor.

Table 3 shows the range of currents that can be measured for various distances between the conductor and the magnetic circuit. The MSM element is triggered and begins to elongate when the current amplitude reaches a value, $I_{trigg}$, but it still does not follow current changes for this value. That happens for the values above $I_{min}$. It saturates and does not change its shape any more for the currents above $I_{max}$. The data in table 3 provide a better insight about the required size of the magnetic concentrator depending on the range of currents that need to be measured.

The next step was to change the value of the circuit's width $w$ and determine the variation of flux densities, $B_{surface}$ and $B_{max}$. The same procedure was then repeated for parameter $t$. The results obtained are presented in tables 4 and 5, respectively. It can be concluded that a narrow magnetic circuit is more sensitive but at the same time it also saturates more easily. On the other hand, a wide magnetic circuit is not a good option either for two reasons: it would increase the size of the NCIT and its cost. Therefore, it is necessary to find a trade-off with respect to the magnetic circuit width, $w$. The value $w = 20$ mm was found to be a suitable size.

$B_{surface}$ (%) and $B_{max}$ in magnetic circuit (%) show a percentage change in comparison to the case when the magnetic circuit is the narrowest ($w = 5$ mm).

The data presented in table 5 show that tapering the poles of the magnetic circuit increases magnetic flux density on the MSM surface significantly for the given geometry compared to the non-tapered circuit. However, the results also show that the level of tapering does not influence the sensitivity significantly. Nevertheless, tapering is recommended as much as geometry allows it. For the given geometry, the approximate value of $t = 35$ mm could be chosen.

3

**Table 2.** Magnetic flux density changes on the surface of the MSM element and in the magnetic circuit with the size of the airgap.

| $w$ (mm) | $t$ (mm) | $r$ (mm) | Airgap (mm) | $B_{surface}$ (T) | $B_{surface}$ (%) | $B_{max}$ in magnetic circuit (T) | $B_{max}$ in magnetic circuit (%) |
|---|---|---|---|---|---|---|---|
| 20 | 60 | 80 | 0.1 | 0.116 | 0 | 1.089 | 0 |
| 20 | 60 | 80 | 0.2 | 0.100 | −13.5 | 1.047 | −3.5 |
| 20 | 60 | 80 | 0.3 | 0.088 | −23.4 | 1.054 | −3.0 |
| 20 | 60 | 80 | 0.5 | 0.073 | −37.4 | 1.011 | −6.8 |
| 20 | 60 | 80 | 1 | 0.051 | −56.4 | 0.983 | −9.5 |

$I_{amp} = 400$ A, $f = 50$ Hz

**Table 3.** Measurement range of the current amplitudes for different distances between the conductor and the magnetic circuit.

| $w$ (mm) | $t$ (mm) | $r$ (mm) | $I_{trigg}$ (A) | $I_{min}$ (A) | $I_{max}$ (A) |
|---|---|---|---|---|---|
| 10 | 20 | 30 | 240 | 360 | 920 |
| 10 | 20 | 35 | 250 | 390 | 1000 |
| 10 | 20 | 40 | 270 | 420 | 1100 |
| 10 | 20 | 45 | 290 | 450 | 1185 |
| 10 | 20 | 50 | 300 | 460 | 1280 |
| 10 | 20 | 55 | 330 | 490 | 1370 |
| 10 | 20 | 60 | 335 | 530 | 1465 |
| 10 | 20 | 80 | 400 | 640 | 1830 |

**Table 4.** Magnetic flux density changes on the surface of the MSM element and in the magnetic circuit with the width of the magnetic circuit.

| $w$ (mm) | $t$ (mm) | $r$ (mm) | $B_{surface}$ (T) | $B_{surface}$ (%) | $B_{max}$ in magnetic circuit (T) | $B_{max}$ in magnetic circuit (%) |
|---|---|---|---|---|---|---|
| 5 | 35 | 55 | 0.146 | 0 | 1.329 | 0 |
| 10 | 35 | 55 | 0.145 | −0.8 | 1.314 | −1.1 |
| 15 | 35 | 55 | 0.144 | −1.8 | 1.298 | −2.3 |
| 20 | 35 | 55 | 0.142 | −2.8 | 1.290 | −2.9 |
| 25 | 35 | 55 | 0.140 | −4.2 | 1.285 | −3.3 |
| 30 | 35 | 55 | 0.138 | −5.5 | 1.271 | −4.3 |

$I_{amp} = 400$ A, $f = 50$ Hz

**Table 5.** Magnetic flux density changes on the surface of the MSM element and in the magnetic circuit with the tapering distance.

| $w$ (mm) | $t$ (mm) | $r$ (mm) | $B_{surface}$ (mT) | $B_{surface}$ (%) | $B_{max}$ in magnetic circuit (T) | $B_{max}$ in magnetic circuit (%) |
|---|---|---|---|---|---|---|
| 20 | 5 | 55 | 113.12 | 0 | 1.307 | 0 |
| 20 | 10 | 55 | 127.56 | 12.8 | 1.295 | −0.9 |
| 20 | 15 | 55 | 133.87 | 18.3 | 1.289 | −1.4 |
| 20 | 20 | 55 | 137.22 | 21.3 | 1.292 | −1.2 |
| 20 | 25 | 55 | 139.44 | 23.3 | 1.286 | −1.7 |
| 20 | 30 | 55 | 140.87 | 24.5 | 1.286 | −1.6 |
| 20 | 35 | 55 | 141.90 | 25.4 | 1.290 | −1.3 |

$I_{amp} = 400$ A, $f = 50$ Hz

Similar to the previous tables, $B_{surface}$ (%) and $B_{max}$ in magnetic circuit (%) show a percentage change in comparison to the case when the level of tapering is smallest ($t = 5$ mm).

# 4. Development of finite element models and estimation of modelling errors

We used ANSYS APDL, a finite element (FE) software tool to develop the model of the conductor, MSM element and the magnetic circuit. The whole model consists of five different materials (MSM alloy, Hiperco50, aluminium, steel and air). Plane53 was chosen for modelling, an eight-node element based on the magnetic vector potential formulation. It has a nonlinear magnetic capability for modelling B–H curves. ANSYS Mesh Tool was used to create the mesh. The mesh was refined in the most sensitive areas such as in the magnetic circuit and in the airgap between the MSM element and the magnetic circuit poles.

In electromagnetic analysis in ANSYS APDL, by using a macro called EMAGERR, it is possible to calculate the mesh discretisation errors for a given part of the model. Two parameters are used to describe their values: $B_{ei}$—relative error for the magnetic flux density (magnitude) for element $i$ and its normalised value, $B_{nei}$. They are calculated using (1) and (2), respectively,

$$B_{ei} = \frac{1}{n} \sum_{j=1}^{n} |B_j - B_{ij}| \tag{1}$$

where,
$B_j$—nodally averaged magnetic flux density,
$B_{ij}$—magnetic flux density of element $i$ at node $j$.

$$B_{nei} = \frac{B_{ei}}{B_{max}} \tag{2}$$

where,
$B_{max}$—maximum nodally averaged magnetic flux density.

The most critical segment of the model is the airgap between the MSM element and the poles of the magnetic circuit because of its proximity to various materials, and its geometry. Accordingly, the values of $B_{ei}$ and $B_{nei}$ were specifically calculated for the airgap.

However, the obtained results do not take into account errors in continuity of the magnetic field where materials differ. Therefore, it is necessary to evaluate the normal component values of $B$ on the border between two materials. Although these values should be the same, it does not necessarily happen in FEM simulations. To control for error in the model, these values were evaluated between Hiperco 50 in the magnetic
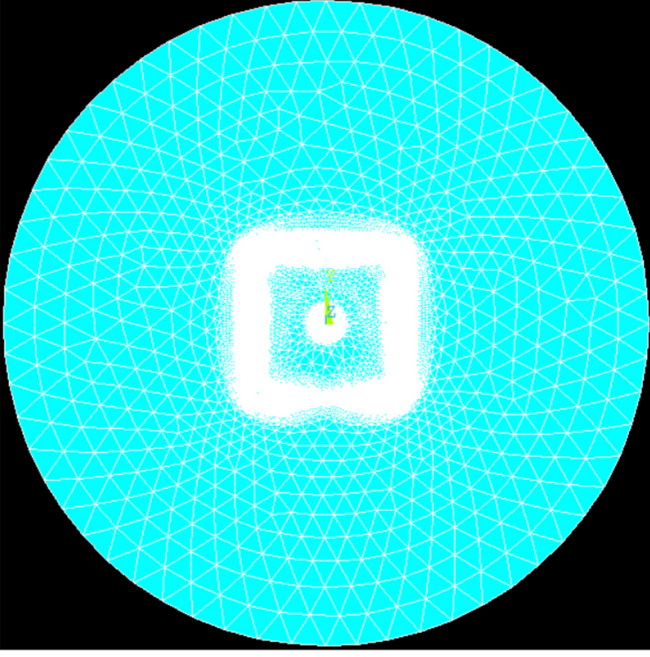
**Figure 2.** Finite element mesh of the rectangular magnetic circuit with rounded corners: $w = 20$ mm, $t = 35$ mm, $r = 55$ mm (full model).
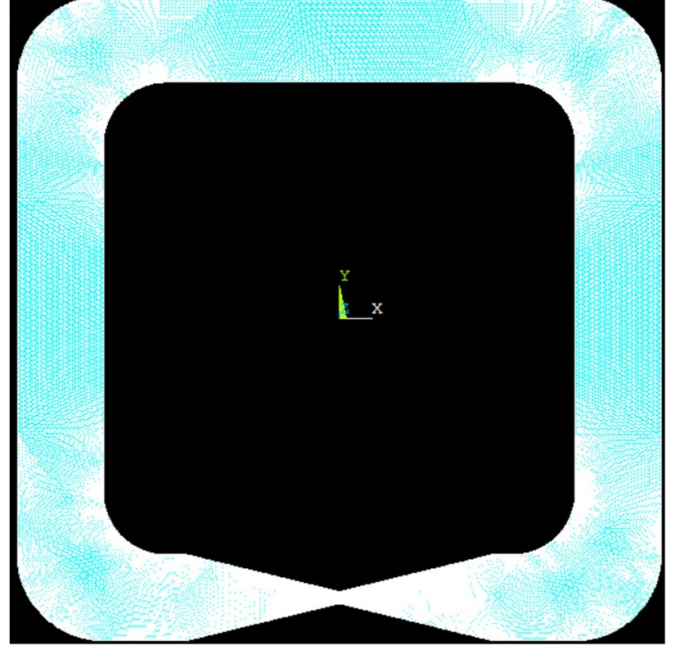


**Figure 3.** Finite element mesh of the rectangular magnetic circuit with rounded corners ($w = 20$ mm, $t = 35$ mm, $r = 55$ mm).

circuit and the air in the airgap. The relative error due to this discontinuity can be calculated using (3):

$$B_{nerr}[\%] = \frac{B_{nair} - B_{nmag}}{B_{nair}} \cdot 100 \qquad (3)$$

where,

$B_{nair}$—normal component of $B$ in the airgap on the interface with the magnetic circuit;

$B_{nmag}$—normal component of $B$ in the magnetic circuit on the interface with the airgap;

The values of the aforementioned parameters depend upon the fineness of the mesh, the given geometry, loads, etc. We developed and tested several models with different levels of mesh refinement.

The mesh of the rectangular magnetic circuit with rounded corners can be seen in figure 2 (here, $I = 400$ A, $w = 20$ mm, $t = 35$ mm, $r = 55$ mm). Figure 3 shows the mesh of the magnetic circuit whereas figure 4 shows the part of the mesh where the MSM element is placed.

The results showed that the maximum value of $B_{nei}$ for this part was $B_{nei(max)} = 0.08824$ with discontinuity on the interface being $B_{nerr} = 0.66\%$. The model had 286 188 FE elements in total out of which 95 448 were in the airgaps between the MSM element and the poles of the magnetic circuit. This refined mesh was chosen to take into account the small airgap and the accuracy requirements for flux density calculation. Increase in the fineness of the mesh especially influences the value of $B_{nerr}$. For example, its range was from $B_{nerr} = 13.56\%$ for the relatively rough mesh having 14 962 elements in total and only 525 elements in the airgap to $B_{nerr} = 0.66\%$ for the case described above. The parameter $B_{nei}$ took values from 0.088 to 0.101 for the same range. Although it can be argued

that the mesh was very fine and that there was a large number of elements in the model, it should be mentioned as an example that $B_{nerr} = 2.97\%$ was attained with only 46 500 elements in total (14 482 in the airgap). Furthermore, it is important to note that the model's convergence tolerance had a value of 0.001.

## 5. Correlation between the strain of the MSM element and the conductor current

In the previous considerations, the focus was to increase the sensitivity of the proposed NCIT. The sensitivity of the MSM element was not very high at low magnetic field, so it was necessary to add a magnetic circuit to increase the magnetic field through the MSM element to trigger its strain.

However, once the MSM element is triggered there are many other parameters that need to be considered and analysed in order to obtain valid results.

The relative magnetic permeability of an MSM element is not constant. It changes from $\mu_r = 2$, when it is fully contracted and consists only of hard variants, to $\mu_r = 50$, when is fully elongated and consists only of easy variants. It should be mentioned that the maximum value of magnetic permeability is not constant, as it depends on the MSM alloy, with its reported value in the range of 40–210 [21]. In our research, it is assumed to be equal to 50 which corresponds to the data published on official website of the manufacturer of MSM materials, ETO MAGNETIC [16]. During the elongation process, the MSM element consists of variable number of hard and easy variants which results in different values of its magnetic permeability. In [21], it is shown that this change in the magnetic permeability is not linear and its change for different values of strain is presented.
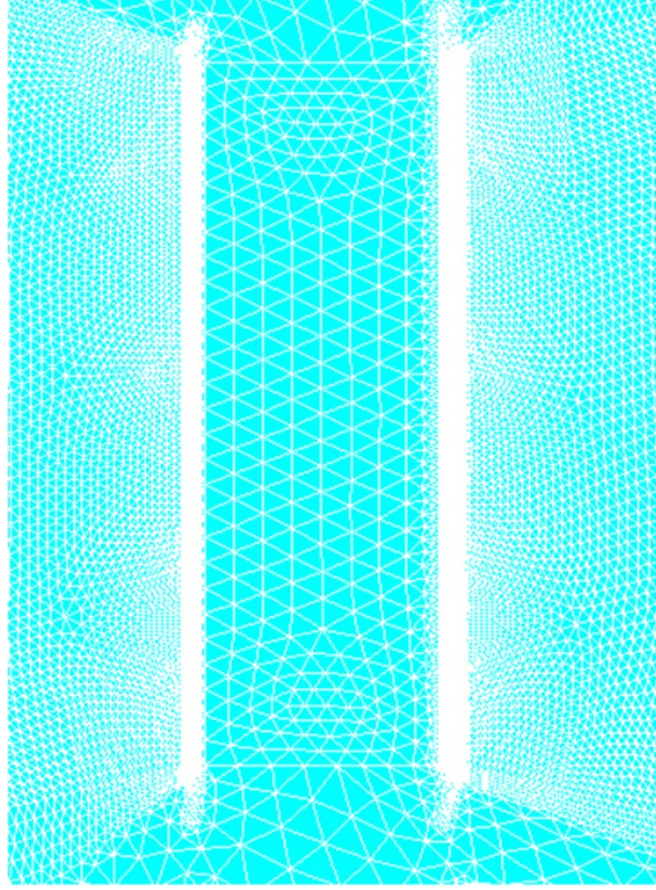
**Figure 4.** Finite element mesh of the MSM element between the poles of the rectangular magnetic circuit with rounded corners ($w = 20$ mm, $t = 35$ mm, $r = 55$ mm).

However, this is not sufficient to establish how the strain of a given MSM element will change with different values of the measured current for a given geometry, which is our goal. The strain-magnetic field relation of magnetic MSM crystals at different pre-stress (load) levels [16] shows the relationship between magnetic flux density on the surface of the MSM element, $B_{surface}$, and its strain, $\varepsilon$. When the current changes, $B_{surface}$ also changes and thus, both the magnetic permeability and the strain of the MSM element will change as well. It is not straightforward to find a relationship between the change of current and the MSM element's strain as the relationship between $B_{surface}$ and MSM's relative magnetic permeability, $\mu_r$ is not known.

This was overcome by assuming the value of $\mu_r$, and then obtaining the values of $B_{surface}$ and checking whether the strain was in accordance with the data obtained in [21] and matched the strain given by data curves in [16]. It was required to repeat this approach for each values of the current used in the simulation. Thus, several hundred simulations were carried out as the values of the amplitude current tested were varied from $290-1400$ A, with a step of 5 A. The results obtained are shown in figures 5 and 6 ($r = 55$ mm, $w = 20$ mm, $t = 35$ mm).

Figure 5 shows the relationship between the amplitude of the current, $I_{amp}$ in the conductor and $B_{surface}$. Finally, the
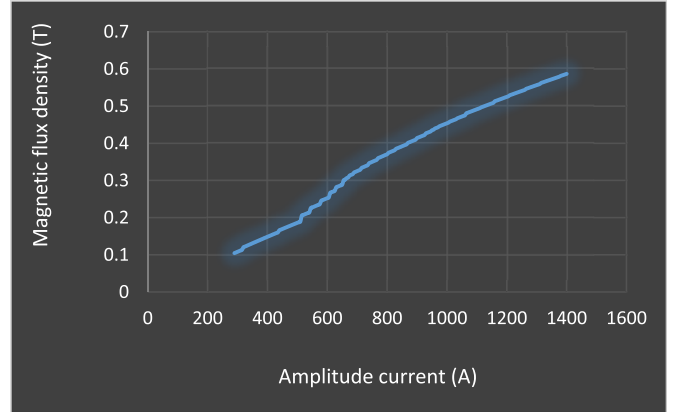


**Figure 5.** Magnetic flux density changes on the surface of the MSM element $B_{surface}$ with amplitude current in the conductor, $I_{amp}$ ($r = 55$ mm, $w = 20$ mm, $t = 35$ mm).

relationship between the amplitude current $I_{amp}$ in conductor and strain $\varepsilon$ of the MSM element is shown in figure 6.

Different measurement ranges can be achieved by changing NCIT's designs. The procedures and simulations described above were repeated for several more designs and some of the
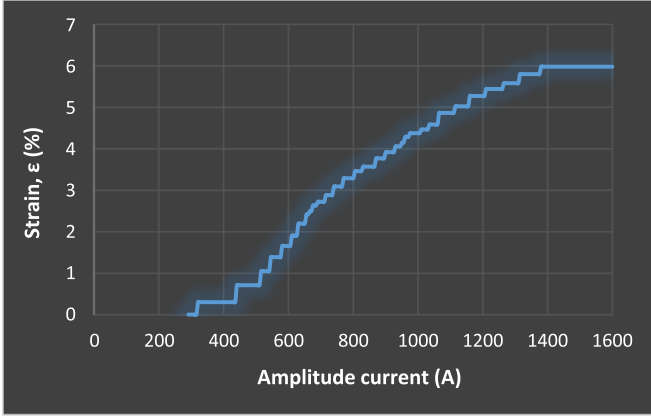
**Figure 6.** Variation of strain of the MSM element $\varepsilon$ with amplitude current in the conductor $I_{amp}$ ($r = 55$ mm, $w = 20$ mm, $t = 35$ mm).
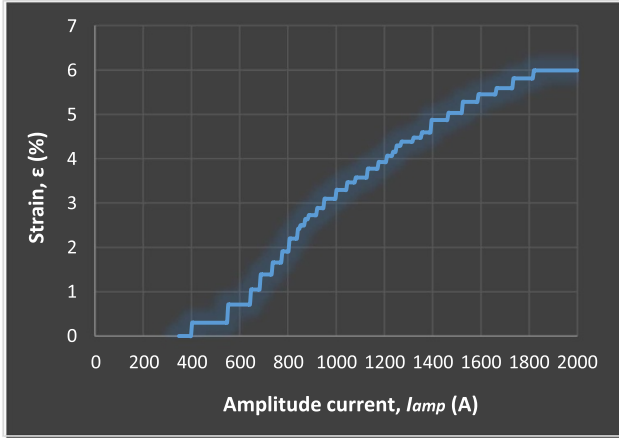


**Figure 7.** Variation of strain of the MSM element, $\varepsilon$ with amplitude current in the conductor $I_{amp}$ ($r = 80$ mm, $w = 20$ mm, $t = 50$ mm).

results can be seen in table 3. Furthermore, as another example, variations of the strain of the MSM element with amplitude current in the conductor for the magnetic circuit with characteristics $r = 80$ mm, $w = 20$ mm, $t = 50$ mm are shown in figure 7.

## 6. Discussion and conclusions

In this paper, we presented a novel approach for current measurement using MSM smart alloys. Significant changes that take place within an MSM element during its elongation have been taken into account and correlation between its strain and the current in the conductor was found.

By analysing the graph in figure 6, several conclusions can be made. Besides the point when MSM element saturates, these results show also, more precisely data for the triggering point of the MSM element. It can be seen that an amplitude current of 330 A will trigger the MSM element, but it will start to follow current changes for the amplitudes above 490 A.

Another point that should be noted in [16] is that when the MSM material saturates and it does not elongate any more at all. This is the point when the MSM element consists only of
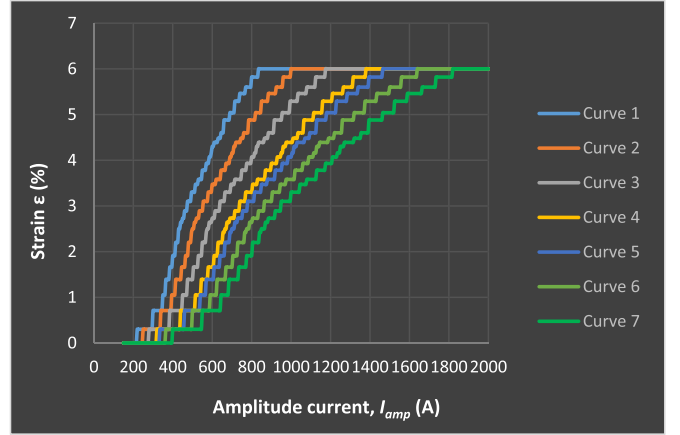


**Figure 8.** Variation of the strain of the MSM element, $\varepsilon$ with amplitude current $I_{amp}$ for various designs of the magnetic circuit (table 6).

**Table 6.** Measurement range of amplitude currents for the various designs of the magnetic circuit.

|  | $r$ (mm) | $w$ (mm) | $t$ (mm) | $I_{trigg}$ (A) | $I_{min}$ (A) | $I_{max}$ (A) |
|---|---|---|---|---|---|---|
| Curve 1 | 25 | 10 | 10 | 220 | 345 | 835 |
| Curve 2 | 35 | 10 | 20 | 250 | 390 | 1000 |
| Curve 3 | 45 | 10 | 30 | 290 | 460 | 1175 |
| Curve 4 | 55 | 20 | 35 | 320 | 510 | 1380 |
| Curve 5 | 60 | 20 | 40 | 335 | 535 | 1465 |
| Curve 6 | 70 | 20 | 50 | 365 | 585 | 1640 |
| Curve 7 | 80 | 20 | 50 | 400 | 640 | 1820 |

easy variants and there are no more hard variants that can rotate and thus increase the strain $\varepsilon$. This happens when the amplitude current reaches 1370 A for the given geometry.

It can be seen that in the case of the magnetic circuit with characteristics $r = 80$ mm, $w = 20$ mm, $t = 50$ mm, an amplitude current of 400 A will trigger the MSM element, but it will start to follow current changes for the amplitudes above 640 A. The MSM element saturates when the amplitude current is 1820 A. In comparison to the previously described case ($r = 55$ mm, $w = 20$ mm, $t = 35$ mm), this design provides measuring the wider current range. The MSM element will saturate later ($I_{max} = 1820$ A instead of $I_{max} = 1370$ A), but also only higher currents would be possible to measure ($I_{min} = 550$ A versus $I_{min} = 490$ A).

If this design ($r = 80$ mm, $w = 20$ mm, $t = 50$ mm) is compared to the one presented in table 3 ($r = 80$ mm, $w = 10$ mm, $t = 20$ mm), it can be concluded that tapering the magnetic circuit and changing its width does not influence current range as much as changing its other dimensions, at the first place distance from the current-carrying conductor. Table 3 shows that the measuring range, in that case, would be 640–1830 A.

Several more curves which show the variations of the strain with the current for various designs are presented in figure 8. Their measurement current ranges are shown in table 6.

It should be noted here that the obtained results could be more precise if a smaller step of the current change has been taken in the simulations (it was 5 A). However, decreasing
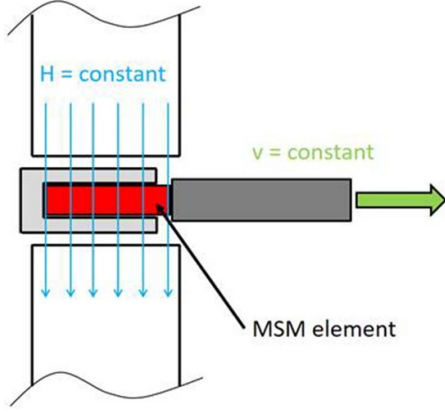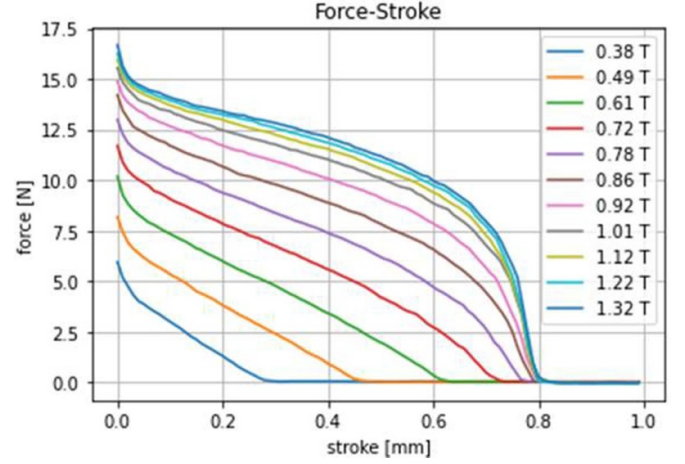
**Figure 9.** The experimental set up.



**Figure 10.** Force–stroke characteristic of MSM element obtained through experiment.

**Table 7.** Comparison between the results obtained in the experiment and in the model.

| $B$ (T) | $\delta_{\mathrm{exp}}$ (mm) | $\varepsilon_{\mathrm{exp}}$ (%) | $\varepsilon_{\mathrm{sim}}$ (%) | Absolute error (strain) (%) | Relative error (strain) (%) |
|---|---|---|---|---|---|
| 0.38 | 0.30 | 2.02 | 1.76 | 0.26 | 13.05 |
| 0.49 | 0.47 | 3.18 | 2.92 | 0.26 | 8.18 |
| 0.61 | 0.63 | 4.24 | 4.4 | −0.16 | −3.86 |
| 0.72 | 0.74 | 4.98 | 5.67 | −0.69 | −13.89 |
| 0.78 | 0.78 | 5.25 | 5.97 | −0.72 | −13.72 |

the current step significantly increases the number of required simulations to be run. Furthermore, the values of $B_{\mathrm{surface}}$, $\mu_{\mathrm{r}}$ and $\varepsilon$ had to be read from the graphs given in [16] and [21] as the data table spreadsheets are not officially published and thus not available. Although that also adds to the inaccuracy of the obtained results, nevertheless, they give a very good idea of the current range that can be measured for the given geometries of the proposed NCITs.

For a commercially available LVDT a linear relationship is specified between the input displacement (a strain of MSM in this case) and the voltage at its output. As this relationship is linear, it is easy to obtain a relationship between the current in the conductor and voltage at LVDT's output and, thus, simply by measuring this voltage it is possible to measure the current inside conductor.

### 6.1. Verification of the developed model

In order to check and validate the methodology we have developed, as well as the obtained results (presented above), we compared them to results obtained through an experiment done by ETO MAGENTIC, the only global manufacturer of MSM materials (provided by courtesy of ETO MAGNETIC, personal communication, 29 April 2022).

In this experiment, a special test bench was used for characterisation of an MSM element. The MSM element was connected to a push rod and exposed to constant magnetic field (figure 9). The push rod is blocked by a linear unit. This linear unit applies a constant slow motion so that the MSM element is able to elongate, making it possible to measure the quasi-static force-stroke characteristic. This procedure was repeated for several different values of magnetic field. A force–stroke characteristic of the MSM element obtained through this experiment is shown in figure 10. The size of the MSM element used in this case was 2.01 mm × 2.85 mm × 14.91 mm.

The points on the curves where the force is zero show the maximum elongation of the MSM element for the applied magnetic field. By reading the values of the MSM's strokes at those points, $\delta_{\mathrm{exp}}$, and knowing the total length of the MSM element (14.91 mm), it is easy to calculate the experimentally obtained strains for those points, $\varepsilon_{\mathrm{exp}}$, using formula:

$$\varepsilon_{\mathrm{exp}}\ [\%] = \frac{\delta_{\mathrm{exp}}}{14.91} \cdot 100. \tag{4}$$

In order to verify our model, we used the same model as described in the previous sections, but this time taking into account the different size of the MSM element used in this experiment and its different strain-magnetic field characteristics which are given in [16] (return path of the yellow curve, load 2N mm$^{-2}$). In our simulations, we would find the value of the current in the conductor that produces the same value of the magnetic field on the surface of the MSM element in the airgap as the value of the magnetic field used in this experiment. Then, by comparing the strain obtained in our model and the strain obtained in this experiment, we are able to make conclusions about the validity of our methodology and hence, the obtained results.

Table 7 shows the comparison between the results obtained in the experiment and in our model. $B$ is magnetic flux density and $\delta_{\mathrm{exp}}$ and $\varepsilon_{\mathrm{exp}}$ are MSM's maximum stroke and maximum strain for the given magnetic field, respectively. $\varepsilon_{\mathrm{sim}}$ is the value of the strain obtained in our model. The last two columns show absolute and relative errors of the strains.

By comparing the experimental results and the results of our model, it can be seen that the model follows the experimental data. As mentioned earlier, the table data of MSM characteristics were not available, which increased the values of the absolute and relative errors. Furthermore, the value of maximum magnetic permeability of the MSM alloy used in the

experiment was $\mu_r = 90$ whereas our model used the value of $\mu_r = 50$ in accordance with the data available for this research. Moreover, magnetic flux density values were rounded to two decimal places in the available data of the experiment, and as a result, so were the values in the analysis of our model. That additionally contributes to the inaccuracy of the results.

Nevertheless, the obtained results show that our model can predict the elongation of the MSM element. Since the same methodology and the same models (with only different MSM element input characteristics) were used in the simulation of the described experiment, and in the above case of the proposed NCIT, it can be concluded that the proposed methodology and the developed model of the NCIT are valid. This example also shows flexibility of the developed model and the possibility to make analyses for different MSM elements.

## Data availability statement

The data that support the findings of this study are available upon reasonable request from the authors.

## Acknowledgments

## ORCID iD

B Nikolic ⓘ https://orcid.org/0000-0002-2656-677X

## References

[1] Metwally I A 2010 Self-integrating Rogowski coil for high-impulse current measurement *IEEE Trans. Instrum. Meas.* **59** 353–60
[2] Kojovic L 2002 PCB Rogowski coils benefit relay protection *IEEE Comput. Appl. Power* **15** 50–53
[3] Kirkham H 2009 Current measurement methods for the smart grid *IEEE PES General Meeting* pp 1–7
[4] Mora J, Díez A, Cruz J L and Andrés M V 2000 A magnetostrictive sensor interrogated by fiber gratings for DC-current and temperature discrimination *IEEE Photonics Technol. Lett.* **12** 1680–2
[5] Lenz J and Edelstein A S 2006 Magnetic sensors and their applications *IEEE Sens. J.* **6** 631–49
[6] Tsai Y P, Chen K L, Chen Y R and Chen N 2014 Multifunctional coreless Hall-effect current transformer for the protection and measurement of power systems *IEEE Trans. Instrum. Meas.* **63** 557–65
[7] Ramsden E 2006 Application-specific sensors *Hall-Effect Sensors: Theory and Application* (Amsterdam: Elsevier) pp 177–85
[8] Nikolić B, Khan S and Gabdullin N 2016 Development of non-conventional instrument transformers (NCIT) using smart materials *J. Phys.: Conf. Ser.* **772** 012065
[9] Nikolić B and Khan S 2018 Modelling of non-conventional instrument transformers (NCIT) by FEM *J. Phys.: Conf. Ser.* **1065** 072046
[10] Nikolić B and Khan S 2019 Modelling and optimisation of design of non-conventional instrument transformers *J. Phys.: Conf. Ser.* **1379** 012057
[11] Murray S J, Marioni M, Allen S M, O'Handley R C and Lograsso T A 2000 6% magnetic-field-induced strain by twin-boundary motion in ferromagnetic Ni–Mn–Ga *Appl. Phys. Lett.* **77** 886–8
[12] Sozinov A, Lanska N, Soroka A and Zou W 2013 12% magnetic field-induced strain in Ni–Mn–Ga-based non-modulated martensite *Appl. Phys. Lett.* **102** 21902
[13] Heczko H S O, Kopecky V, Fekete L, Jurek K, Kopecek J and Straka L 2015 Magnetic domains and twin microstructure of single crystal Ni-Mn-Ga exhibiting magnetic shape memory effect *IEEE Trans. Magn.* **51** 15–18
[14] Pagounis E, Chulist R, Szczerba M J and Laufenberg M 2014 High-temperature magnetic shape memory actuation in a Ni–Mn–Ga single crystal *Scr. Mater.* **83** 29–32
[15] Straka L, Soroka A, Seiner H, Hänninen H and Sozinov A 2012 Temperature dependence of twinning stress of type I and type II twins in 10M modulated Ni–Mn–Ga martensite *Scr. Mater.* **67** 25–28
[16] ETO MAGNETIC Magnetic shape memory technology (MAGNETOSHAPE) (available at: www.etogruppe.com/en/company/magnetoshape-r.html) (Accessed 8 April 2022)
[17] British Standards Institution 2013 BS EN 50182:2001 *Conductors for Overhead Lines—Round Wire Concentric Lay Stranded Conductors* pp 27–74
[18] Lings R, Chartier V and Maruvada P S 2005 Overview of transmission lines above 700 KV *Proc. Inaugural IEEE PES 2005 Conf. and Exposition in Africa* pp 11–15
[19] Liang Z, Li Y, Hu H and China J J 2012 Design of UHVAC transmission line in China Zheng-Ping *Eur. Trans. Electr. Power* **22** 4–16
[20] Bayliss C R and Hardy B J 2012 Overhead line conductor and technical specifications *Transmission and Distribution Electrical Engineering* (Oxford: Newnes) pp 683–750
[21] Gabdullin N 2016 Modelling and design of high-speed, long-lifetime and large-force electromagnetic actuators based on magnetic shape memory alloys *PhD Dissertation* University of London